3D CNT macrostructure synthesis catalyzed by $MgFe_2O_4$ nanoparticles—A study of surface area and spinel inversion influence

Rúbia Young Sun Zampiva[a,*], Claudir Gabriel Kaufmann Junior[a], Juliano Schorne Pinto[b], Priscila Chaves Panta[a,c], Annelise Kopp Alves[a], Carlos Pérez Bergmann[a]

[a] *Department of Materials Engineering, Federal University of Rio Grande do Sul- UFRGS. Osvaldo Aranha 99, Porto Alegre, RS 90035- 190, Brazil*
[b] *Génie Chimique Laboratory INP-ENSIACET. 4 allée Emile Manso, CS 84234, 31432 Tolouse Cedex 4, France*
[c] *La Salle University Center,Av. Victor Barreto 2288, Canoas, RS 92010-000, Brazil*

Keywords:
3D CNT macrostructures
$MgFe_2O_4$ catalyst
Solution combustion synthesis
Spinel inversion
Surface area
van der Waals forces

A B S T R A C T

The $MgFe_2O_4$ spinel exhibits remarkable magnetic properties that open up numerous applications in biomedicine, the environment and catalysis. $MgFe_2O_4$ nanoparticles are excellent catalyst for carbon nanotube (CNT) production. In this work, we proposed to use $MgFe_2O_4$ nanopowder as a catalyst in the production of 3D macroscopic structures based on CNTs. The creation of these nanoengineered 3D architectures remains one of the most important challenges in nanotechnology. These systems have high potential as supercapacitors, catalytic electrodes, artificial muscles and in environmental applications. 3D macrostructures are formed due to an elevated density of CNTs. The quantity and quality of the CNTs are directly related to the catalyst properties. A heat treatment study was performed to produce the most effective catalyst. Factors such as superficial area, spinel inversion, crystallite size, degree of agglomeration and its correlation with van der Waals forces were examined. As result, the ideal catalyst properties for CNT production were determined and high-density 3D CNT macrostructures were produced successfully.

1. Introduction

The magnesium ferrite ($MgFe_2O_4$) spinel is a ceramic oxide with a face-centered cubic crystalline system. The general structure of spinels consists of divalent ions surrounded by oxygens forming tetrahedral sites, and trivalent ions surrounded by oxygen forming octahedral sites [1]. However, depending on the synthesis route or conditions, $MgFe_2O_4$ does not strictly follow this structural pattern. Its structural configuration becomes a partially inverse spinel. The tetrahedral sites are partially filled by trivalent metal ions, and the octahedral sites are partially filled by divalent ions. Spinel position inversion directly affects the physicochemical properties of the ferrite [2,3]. Since magnesium has a covalent character and oxygen has negligible mobility, iron presents the higher mobility in the magnesium ferrite structure [4,5].

Synthetic $MgFe_2O_4$ nanoparticles are produced by a variety of techniques such as coprecipitation [6], sol-gel [7], hydrothermal route [8], microemulsion [9], and solution combustion synthesis (SCS). SCS is a low cost, fast technique that produces high amounts of nanoparticles with high purity and structural homogeneity [10–12]. The SCS consists of precursors dissolved in aqueous medium (usually metallic nitrates) [13] and a complexing agent (fuel) such as citric acid [14]; oxalic acid, glycine [15], and urea [16]. The solution is heated to 400 °C to initiate the fuel self-ignition and produce nanoparticles from the solution constituents. The self-sustaining ignition temperature is between 150 °C and 500 °C. With combustion, it can reach more than 1700 °C [17]. A highly crystalline and deagglomerated solid product is formed at the end of the process [18].

Many studies on ferrites nanoparticles including $MgFe_2O_4$ spinel have been recently described due to their distinct magnetic properties, which open up numerous application possibilities including cancer treatment [19,20], biosensors [21] and water purification [22]. $MgFe_2O_4$ has also been used as a catalyst in the production of carbon structures such as carbon nanotubes (CNT). In CNT studies, spinels are usually based on metal catalysts (Ni, Co, Mo, Fe . . .) and are supported by oxides (MgO, Al_2O_3, SiO_2 and CaO) [23–25]. Magnesium ferrite spinel is an excellent catalyst for

* Corresponding author.
E-mail addresses: rubiayoungsun@gmail.com (R.Y.S. Zampiva), gabrielklpgodines@gmail.com (C.G. Kaufmann Junior), jschornpinto@gmail.com (J.S. Pinto), pr.priscila@gmail.com (P.C. Panta), anelise.alves@ufrgs.br (A.K. Alves), bergmann@ufrgs.br (C.P. Bergmann).

multiwall CNT (MWCNT) production. $FeMg_2O_4$ when applied as a catalyst is often represented in the literature by Fe/MgO system [26–28]. This is because metallic Fe^{3+} ions are the active catalyst in the synthesis process, while MgO acts as the dispersant of Fe^{3+} ions (support) [28].

The concentration of metallic ions (stoichiometry) and the catalyst powder morphology (crystallite size, agglomeration and surface area) directly influence the properties (density, quality and morphology) of the resulting carbon structures [29–31]. An interesting possibility is the production of 3D macroscopic carbon structures based on solid catalyst nanoparticles. The creation of such a nanoengineered 3D architecture remains one of the most important challenges in nanotechnology. The production of nanoengineered 3D carbon structures with controlled density and architecture is one of the most desirable steps for building next-generation carbon-based functional materials [32]. These structures have potential application in areas such as supercapacitors [33], catalytic electrodes, dry adhesion [34], artificial muscles [35], gas absorbers [36] and environmental applications [37–39].

Aiming the obtention of 3D CNT structures, different techniques are reported in the literature, but basically, these involve CVD or CNT functionalization processes [31,36–41]. Most part of the studies based on CVD works with catalysts in solution, commonly ferrocene [36,37,40]. However, it is known that the CVD technique allows the use of different types of liquid and solid catalysts. There is no universal consensus regarding the nucleation and growth model of CNTs. However, the most accepted model so far has been proposed by Baker et al. [42]. This explains the growth of CNTs by the catalytic dissociation of a carbon source on the particles of a specific catalyst.

3D carbon macrostructures are formed with an elevated density of CNT [37,38]. The yield of CNT is strongly related to the catalyst surface area. Larger surface areas offer more metallic ions for CNT production [29,30]. In this work, the heat treatment temperature of $MgFe_2O_4$ catalysts produced by SCS was varied to obtain the largest surface area. Factors such as crystallite size, degree of agglomeration and their correlation with van der Waals forces were studied. The influence of spinel inversion was also presented. The MWCNTs were synthesized by chemical vapor deposition (CVD) using $MgFe_2O_4$ as catalyst to produce 3D carbon macrostructures.

2. Materials and methods

2.1. Synthesis of MgF_2O_4 nanoparticles catalyst

2.1.1. Materials

$Mg(NO_3)_2{\cdot}6H_2O$ 99% (Sigma Aldrich), $Fe(NO_3)_3.9H_2O$ 99.95% (Sigma Aldrich), glycine 99% (Sigma Aldrich) and distilled H_2O.

2.1.2. Method

The nanopowdered MgF_2O_4 catalyst was produced by SCS. The $Mg(NO_3)_2{\cdot}6H_2O$ and $Fe(NO_3)_3{\cdot}9H_2O$ were employed to produce MgF_2O_4 powder. The nitrates were individually dissolved in water and then mixed. The solution was stirred and heated for approximately 5 min. When reaching 60 °C, the fuel (glycine previously dissolved in water) was added. The precursors/fuel stoichiometry was established via the propellants method [43]. The balanced equation (1) is presented below:

$$2Fe(NO_3)_3 \cdot 9H_2O + 1Mg(NO_2)_3 \cdot 6H_2O + 0,20C_2H_2NO_2 \quad (1)$$

The temperature and stirring were maintained for few minutes to promote perfect homogenization. The solution was inserted into an electric furnace (muffle) preheated to 400 °C until complete combustion (around 15 min). No grinding process was used.

Table 1
$MgFe_2O_4$ heat treatment temperatures.

Sample	*Calcination temperature (°C)*
Ct0	–
Ct1	500
Ct2	700
Ct3	900
Ct4	1100
Ct5	1200

Table 2
$MgFe_2O_4$ catalysts and their respective CNTs samples.

$MgFe_2O_4$ catalyst	*CVD produced samples*
CT0	CNT0
CT1	CNT1
CT2	CNT2
CT3	CNT3
CT4	CNT4
CT5	CNT5

The sample was treated at different temperatures as described in Table 1.

2.2. Synthesis of the CNT 3D structures

2.2.1. Materials

$MgFe_2O_4$, Ar 99.999% (Sigma Aldrich), H_2 99.95% and ethylene 99.99% (Sigma Aldrich).

2.2.2. Method

To study the catalyst influence, we established a standard methodology that varied only one, the catalyst. The samples were produced employing a CVD system. An alumina boat with $MgFe_2O_4$ (0,100 g) was inserted in a furnace (Jung, model LT3-9013) with a silicon glass tubular chamber. The furnace was heated to 850 °C (50 °C/min) with continuous Ar flow (300 cm^3/min) and then held for 45 min. At 850 °C, the H_2 valve was opened (30 cm^3/min). After 15 min, the Ar valve was closed, ethylene valve was opened (30 cm^3/min), and the H_2 valve was kept opened until the final of the plateau. When the system started to cool down, the ethylene valve was closed, the Ar valve was opened and the H_2 remained open until 500 °C. At this temperature, the H_2 and the ethylene were closed, and the Ar flow was kept opened until 100 °C. The alumina boat was removed from the furnace at 100 °C. The catalyst samples calcined at different temperatures were employed to produce the MWCNT. The resulting samples are described in Table 2.

2.3. Chemical and structural characterization

The crystallinity of the sample was evaluated by X-ray diffraction (XRD) using a PHILIPS diffractometer (model X'Pert MPD), 40 kV, 40 mA and Cu anode. The powders crystallite size were calculated by Scherrer's equation (eq. (1)):

$$D_p = \frac{K\lambda}{\beta_{1/2} COS\theta} \quad (1)$$

In this equation, D represents the crystallite size, K is a constant whose value depends on the particle shape (we assume the particles to be spherical, so K=0.94), λ is the wavelength of the used electromagnetic radiation (1.5406 Å, value related to the characteristic main radiation emitted by copper), θ is the Bragg's angle and β is the contribution of the crystallite size to the full width at half maximum (FWHM) of the diffraction peak correspondent in radians. The surface areas of the catalysts were obtained by nitrogen absorption method (BET- Quanta Chrome, Nova-1000 model).

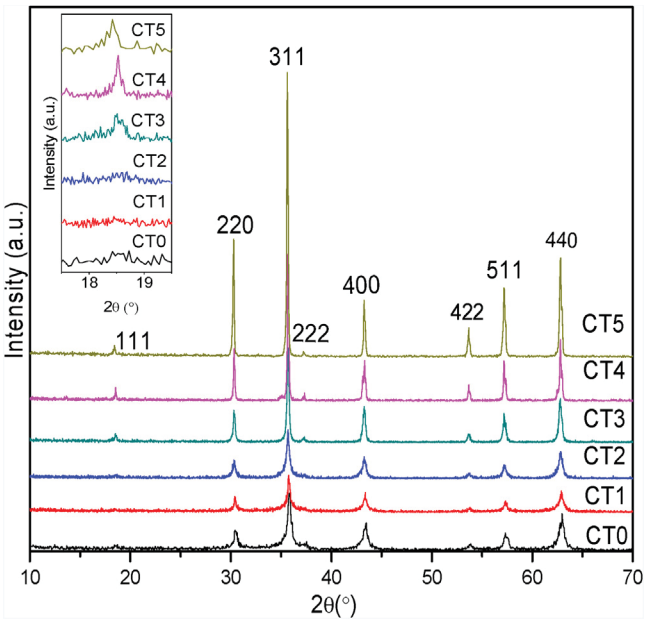

Fig. 1. Heat treated nanopowders diffractogram. The box in the upper left side shows the 17.5°-19.5° area magnified.

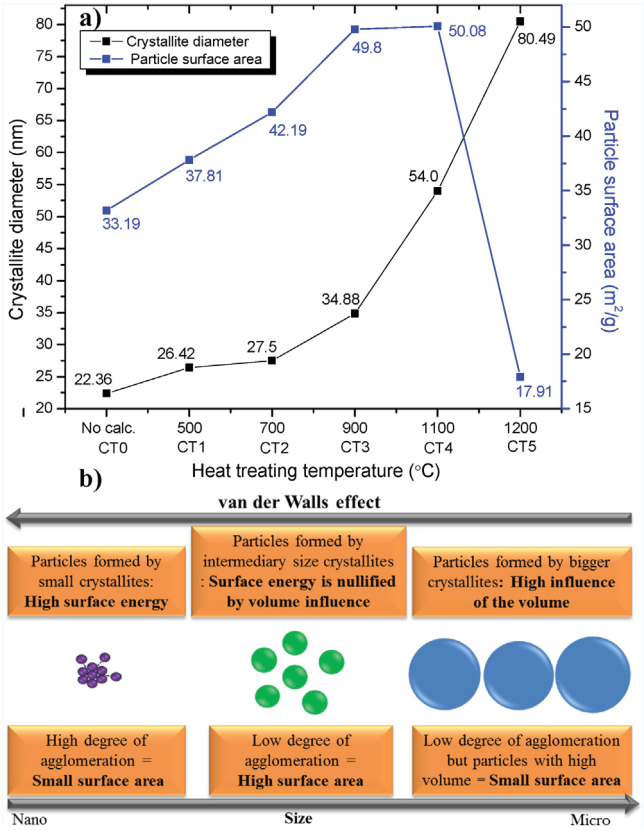

Fig. 2. a) Crystallite size (in black) and particle surface area (in blue) variation with the temperature of heat treatment. The samples were analyzed straight after synthesis. No grinding process was used. CT0 to CT4 presented the increasing of particle surface area with the crystallite size. Sample CT5 presented the decreasing of particle surface area with crystallite size increasing. b) Representative scheme of the relation between particle surface area, crystallite size and van der Waals forces. (For interpretation of the references to colour in this figure legend, the reader is referred to the web version of this article.)

Changes on chemical and structural composition during the heat treatment were studied via thermogravimetry on a Netzsch 449 DSC/TG thermal analysis system. The $MgFe_2O_4$ morphology was characterized by scanning electron microscopy (SEM) in a JEOL microscope (JSM 6060) with a maximum operational tension of 30 kV and nominal resolution of 3.5 nm. The applied tension was 10–20 kV. The $MgFe_2O_4$ and CNT high resolution transmission electron microscopy (HRTEM) used a JEOL microscope (JEM 2010) operating between 80 kV and 100 kV with punctual resolution of 0.45 nm and line resolution of 0.20 nm. The quality and density of CNTs production were analyzed by Raman spectroscopy using a Renishaw inVia microRaman System with a laser wavelength of 532 nm focused onto the sample with a 50 × objective lens. Nitrogen adsorption/desorption isotherms are used to investigate the Brunauer, Emmett, and Teller (BET) surface area and Barrett-Joyner-Halenda (BJH) pore size. These surface structure parameters were obtained using an automated surface area analyzer (Autosorb Quantachrome –NOVA 1000e-Gas Adsorption Surface Area and Pore Size Analyzer). BET was performed to the nanopowder catalyst and BET-BJH was carried out to the NTC sponge. The NTC bulk density and porosity percentage were analyzed by Archimedes method [44].

3. Results and discussion

3.1. $MgFe_2O_4$ nanoparticles

The diffractogram (Fig. 1) shows characteristic crystalline peaks only for magnesium ferrite phase at all temperatures of heat treatment according to JCPDS 73–1960. This indicates the purity and homogeneity of the samples produced by SCS. As the temperature increases, the peaks becomes more intense and sharper, which is related to crystallinity and increasing crystallite size. The crystallite sizes calculated by the Scherrer's equation are shown in Fig. 2a. Even at the highest temperature of heat treatment, the crystallite size remained at the scale of dozen nanometers. This phenomenon is related to the covalent character of magnesium, which makes crystallization more difficult and leads to smaller crystallites [45].

Interestingly, peak 111 appears for samples CT3, CT4 and CT5 treated above 900 °C, as better shown in the diffractogram amplified box. This peak is directly related to the structure disorder degree [5]. In the literature, the disorder that occurs at 957 °C is described as the change from magnesium ferrite α to γ [46]. As temperature increases, more energy is available for the elements to diffuse in the structure leading to order-disorder phase or to normal-inverse spinel transitions [5,47].

Surface area is one of the most important parameters in catalytic nanoparticles. Large surface areas provide more active ions for catalysis and increase reaction rates [48,49]. Particles are composed of 2 or more single crystals (crystallites). The total surface area of a particulate sample and the size of the crystallites in the particles are usually inversely proportional. Smaller crystallites form smaller particles with higher surface area. However when the behavior is studied at the nanoscale (< 1 μm), both can grow in the same direction [50–52]. As crystallite size decreases, the cohesiveness of the powder (the strength of the forces that cause agglomeration) increases [53]. Thus nanoparticles tend to agglomerate and form larger particles with less surface area. This phenomenon is observed in Fig. 2a where the increasing crystallite size from sample CT0 to CT4 increased the particle surface area.

The increasing of the surface area and crystallite size to the same direction occurs due to the influence of forces like van der Waals that are predominant in interactions between the surfaces of nanoscale particles: Smaller particles have higher surface energy. These particles tend to agglomerate to balance the entropy forces [53–55]. A representative scheme of the relation between particle surface area, crystallite size and van der Waals forces is shown in

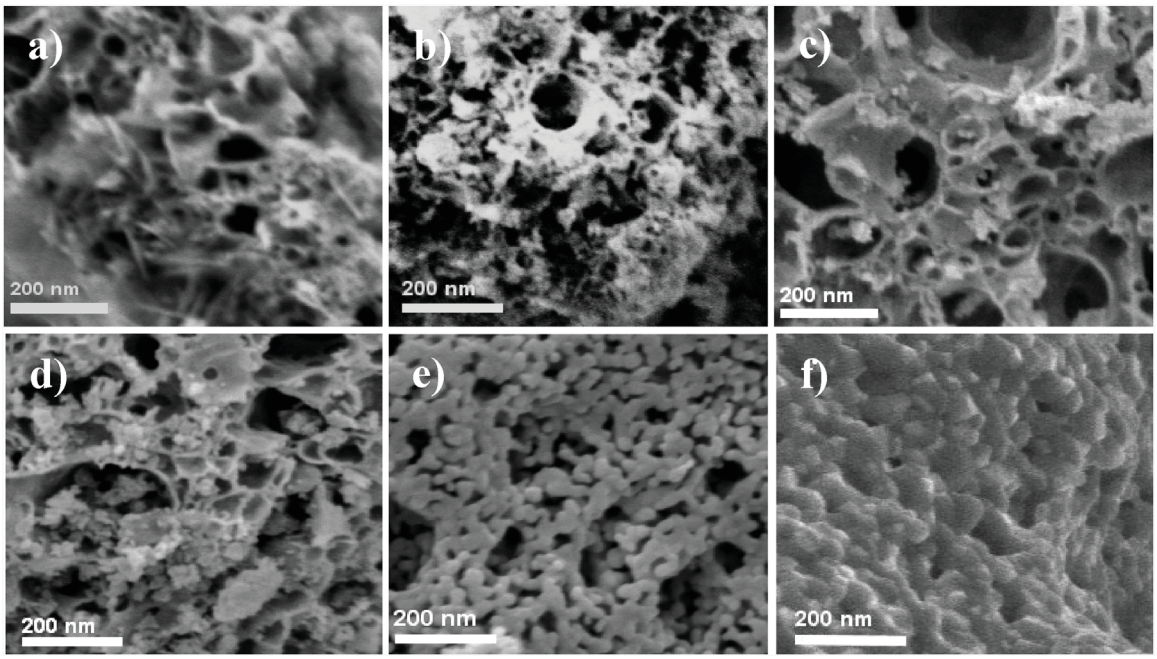

Fig. 3. SEM images of the samples. The nanoparticles formed structures with large porous at a) CT0, b) CT1, c) CT2, d) CT3. Samples e) CT4 and f) CT5 presented distinct morphology.

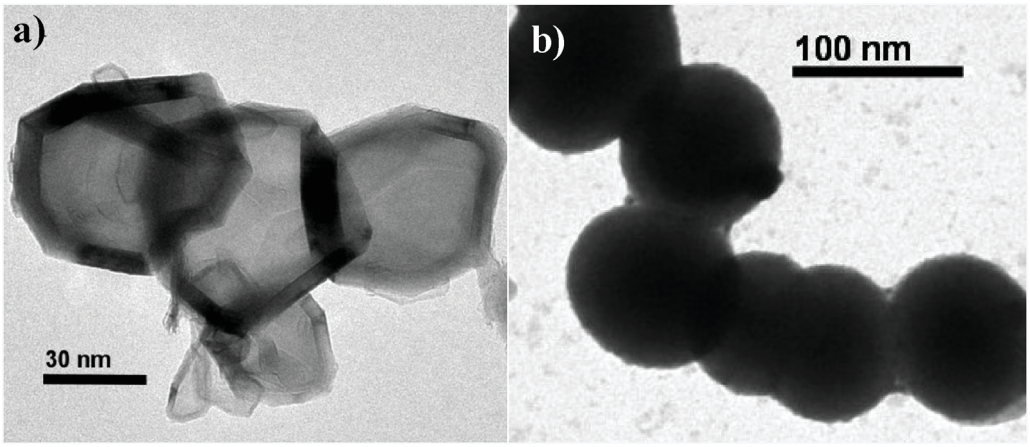

Fig. 4. TEM images a) CT3 nanoparticles; crystallites around 30 nm are observed in the particles and b) CT4 nanospheres; the spheres presented a higher particle size compared to the CT3 particles.

Fig. 2b. The smaller the crystallites in the particle, the higher particle surface area influence. As the crystallite size increases, the surface energy becomes less representative compared to the influence of the particle volume. Diminishing the van der Waals forces interactions, the tendency of agglomeration is reduced. This increases the total sample surface area, however in a high volume particle, much of the sample becomes unavailable at the particle surface [56,57]. This reduces the total sample surface area available for catalysis, as shown to sample CT5 (Fig. 2a).

At a scale of a few dozen of nanometers, the reduction of the particle size did not increase the sample surface area, due the particles agglomeration. At higher scale sizes, the sample lost surface area due the particle volume. The ideal catalyst particle size is an intermediary value between the smallest possible volume and the smallest agglomeration degree. The micrographs (Fig. 3a, b, c and d) sequentially show the variation of the porous structures formed by the nanoparticle agglomerates with increasing porosity as the heat treating temperature increases (CT0-CT3).

The samples CT4 and CT5 (Fig. 3c and f) presented a distinct morphology compared to the rest of the samples. This morphologic alteration is explained by the increasing of diffusion at high temperatures. Above 957 °C, the diffusion energy is extremely high [58,4,5]. With increasing ionic movement, the ions tend to migrate to lower total free energy states through the free surface energy reduction. This causes the nanoparticles to form nanospheres [59,60]. This change is clearly observed in the transmission micrograph shown in Fig. 4a and b.

The nanospheres at CT4 have higher crystallite and particle size compared to the CT3 nanoparticles, according to XRD and TEM, however they have a higher degree of deagglomeration, which kept higher surface area value to CT4 (Fig. 2a CT3 and CT4). CT5 is also formed by nanospheres, however at 1200 °C the diffusion is sufficient to promote particles coalescence and the formation of large sintered structures, which decreased the available surface area (Fig. 2a CT5).

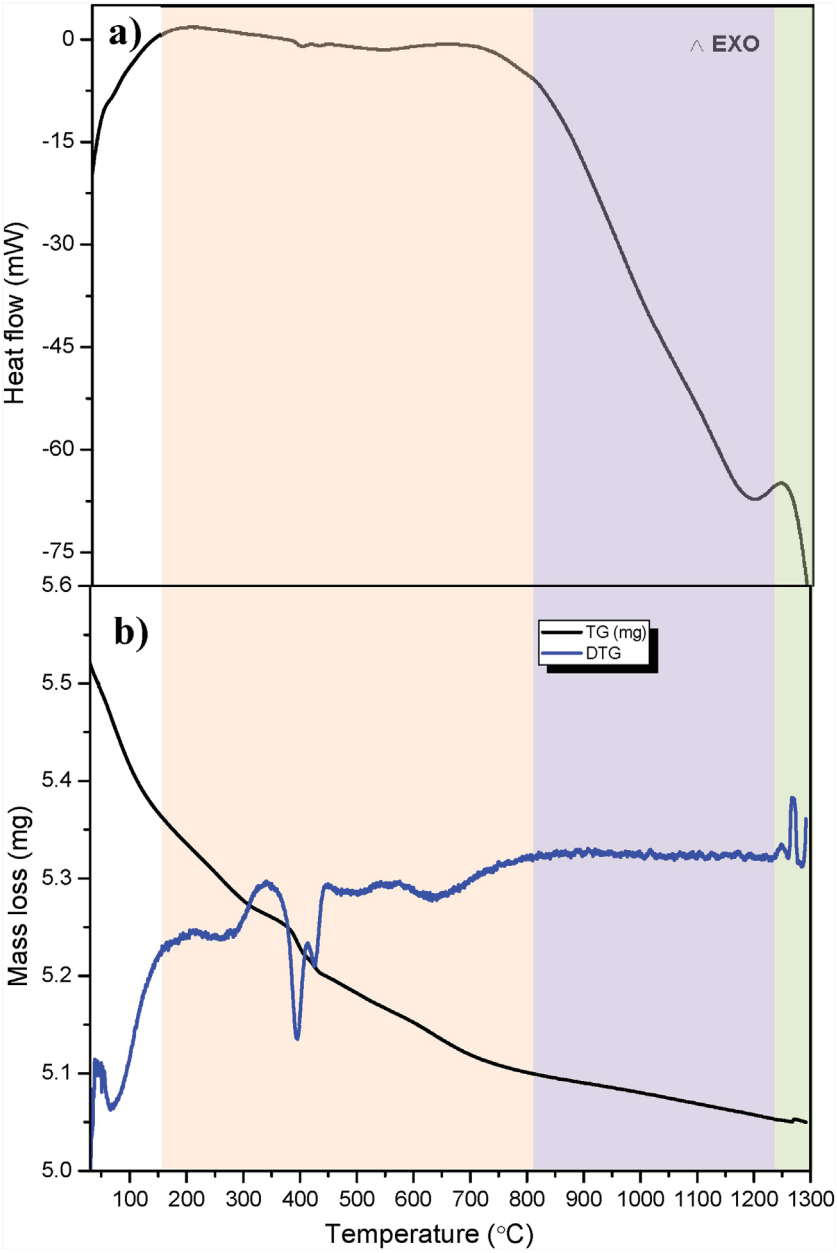

Fig. 5. CT0 Thermogravimetric analysis of a) DSC and b) TG (black line) and DTG (blue line). The white area represents the dehydration temperature, orange area presents the magnetic structural variation temperature, the purple area indicates the temperature of gradual structural disorder increasing and coalescence, and the green area is the temperature of phase decomposition. (For interpretation of the references to colour in this figure legend, the reader is referred to the web version of this article.)

Thermogravimetric analysis (Fig. 5a and b) shows a mass loss around 100 °C due the sample dehydration. There are endothermic and exothermic peaks related to the magnetic reversible and irreversible structural changes such as Curie point between 200 and 800 °C (Fig. 5 orange area) [5]. The small exothermic peak around 450 °C may be related to decomposition of a minimum organic residue [61]. The endothermic heat flow between 800 °C and 1250 °C has no mass loss (Fig. 5 purple area), and this is related to the increasing ionic mobility in the spinel structure [4]. Above 1050 °C, literature indicates the sintering process of ferrite magnesium, due to particle coalescence, reaching a maximum value around 1250 °C [58]. Above this temperature (Fig. 5 green area), the exothermic peaks are related to initial $MgFe_2O_4$ decomposition into α-Fe_2O_3 and MgO phases [62].

3.2. MWCNT and 3D macrostructures synthesis

Raman spectra of the CVD produced samples (Fig. 6) show MWCNT characteristics D, G and G‘ bands at 1342, 1572 cm^{-1} and 2738 cm^{-1}, respectively [63,64]. The G‘ band specifies the MWCNT purity degree [63]. The MWCNT have a higher G’ band intensity than D and G bands. Higher MWCNT purity implies fewer amorphous carbons and defects. MWCNT quality and quantity is also measured by the (I_D/I_G) ratio. This ratio is related to the carbon graphitization degree (conversion of amorphous, semi-ordered or free carbon into three-dimensionally ordered graphitic structure)[65]. An elevated graphitization degree means high quality and quantity of CNT. [64]. The lower the (I_D/I_G) ratio, the higher the graphitization degree.

CNT0 showed a higher (I_D/I_G) ratio than the other samples. This result is justified by the tendency of catalysts powders with high agglomeration degree and low surface area to produce amorphous

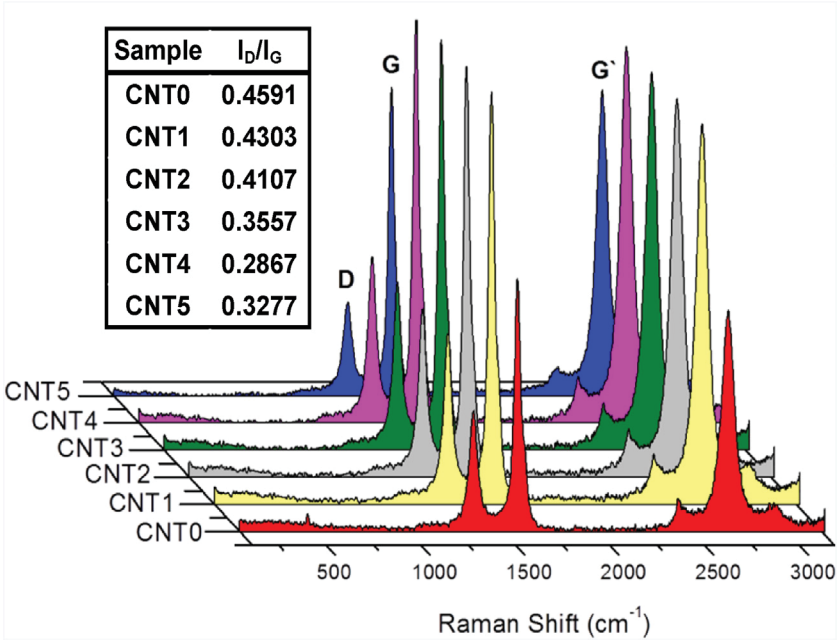

Fig. 6. Raman spectroscopy of the MWCNT samples. The (I_D/I_G) ratio is presented in the box.

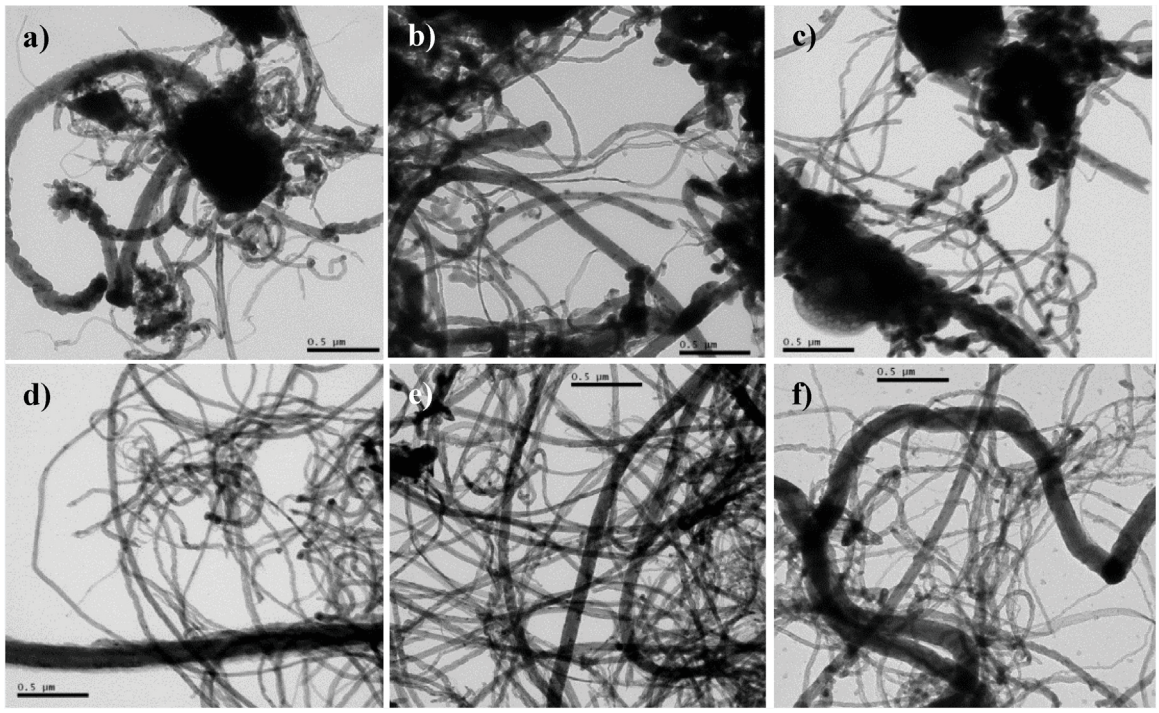

Fig. 7. TEM images of the produced MWCNT. a) CNT0, b) CNT1, c) CNT2 d) CNT3, e) CNT4 and f) CNT5.

carbon and low density of MWCNT [29–31]. With the increasing of heat treating temperature, the catalyst surface area and crystallinity increased too. This directly influenced the MWCNT sample production as shown in the Raman spectra. The (I_D/I_G) ratio decrease with increasing catalyst surface area.

This phenomenon is demonstrated in the MWCNT TEM micrographs Fig. 7a to Fig. 7f. A gradual increasing of MWCNT quality and homogeneity with the increasing of carbon graphitization degree is observed. The CNT0, CNT1 and CNT2 micrographs (Fig. 7a, b and c) presented the formation of a few MWCNT clusters and others carbon based structures. It is observed high particulates in the samples. The elevated particle agglomeration led to a reduced number of catalytic ions available during the MWCNT synthesis. The MWCNT production was reduced. CNT3 (Fig. 7d) showed specific areas with high density of MWCNT and no presence of high particulates. CNT4 (Fig. 7e) has an elevated density of homogenous MWCNT in all sample, with no high particulates observed. Larger catalyst surface area implies more catalytic ions available for carbon graphitization. This leads to higher density of MWCNT production [31,65]. Sample CNT5 (Fig. 7f) presented a reduced MWCNT production. Few clusters of MWCNTs were observed.

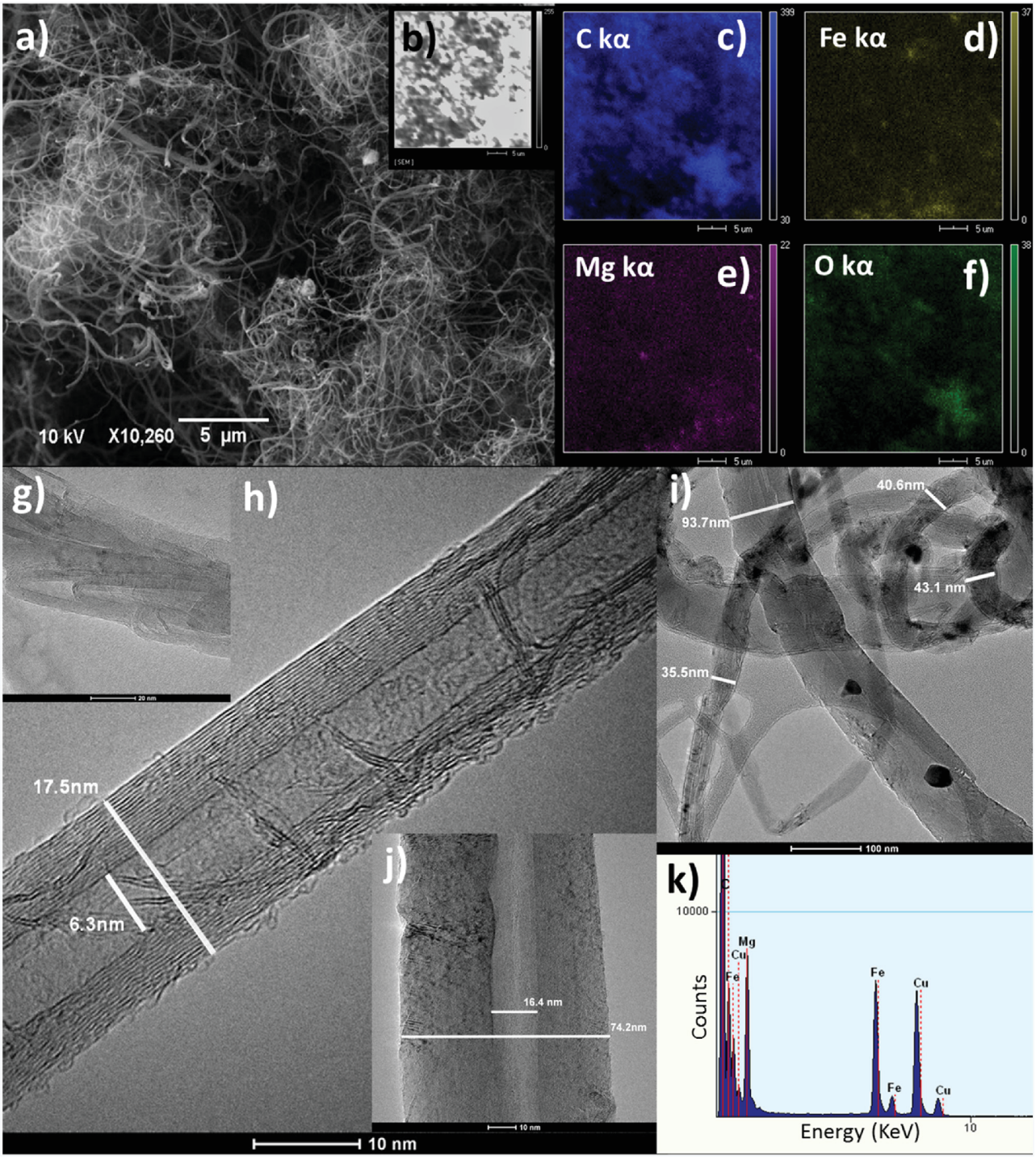

Fig. 8. a) NTC4 SEM micrograph showing the entangled nanotubes, b) SEM of the area analyzed by EDS; EDS mapping of c) carbon d) iron e) magnesium and f) oxygen; NTC4 HRTEM presenting g) MWCNT growing agglomerated to the same direction; h) Single MWCNT with 17.5 nm of external diameter and 6.3 nm of internal diameter, the walls structure are well observed; j) single MWCNT with 74.2 nm of external diameter and 16.4 nm of internal diameter and i) TEM image showing the catalyst particles in the tubes structure.

Although all the samples showed the formation of MWCNT, only the CNT4 (with the highest graphitization degree) had sufficient production to generate a well-defined 3D macrostructure. Fig. 8a shows the SEM micrograph of the CNT4. It is observed the formation of a dense entanglement of MWCNT and also the presence of some particles distributed in the sample. Fig. 8b shows a SEM image of the area mapped by EDS; Fig. 8c, d, e and f, present the EDS mapping of C, Fe, Mg and O respectively. Since Mg and Fe have similar distribution in the sample, the particles in the SEM image might be related to the $MgFe_2O_4$ catalyst and its distribution throughout the sample indicates the multidirectional formation of CNT generated from the catalyst particles.

After the synthesis, part of the nanoparticles remains in the nanotubes structure, as observed in Fig. 8i. An EDS analysis (Fig. 8k) was performed for the area presented in Fig. 8i; peaks of Mg, Fe, O, C and Cu are observed in the spectra. The ions Mg, Fe, O are related to the $MgFe_2O_4$ nanoparticles in the MWCNT, C to the MWCNT and Cu is due the sample holder composition. Fig. 8 h and 8 j present two

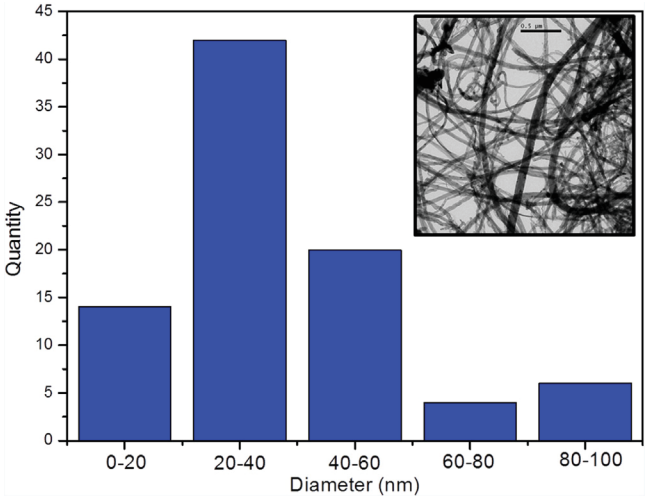

Fig. 9. Histogram of the diameter distribution of MWCNT in the sample CNT4, at the left side, the CNT4 TEM image.

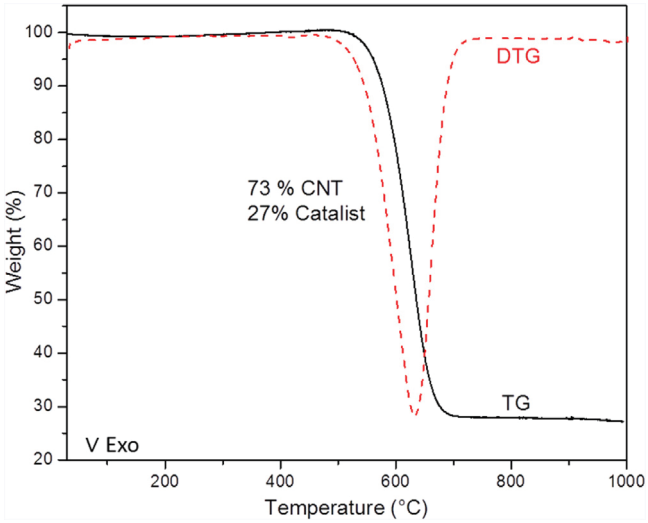

Fig. 10. CNT4 thermogravimetric analysis of TG (black line) and DTG (red dotted line). The curves behavior around 650 °C are related to MWCNT decomposition. (For interpretation of the references to colour in this figure legend, the reader is referred to the web version of this article.)

MWCNT with an elevated difference in the diameter size, Fig. 8 h have an external diameter of 17.5 nm while the MWCNT in Fig. 8 j have 74.2 nm. Despite this difference, both have a similar tubular structure, presenting in average more than 20 tubular walls. From the solid catalyst, the MWCNT grown in aleatory directions and forms a variety of junctions and curves, as presented in the SEM image (Fig. 8a) as well in the TEM image (Fig. 7e) allowing the formation of high volume macrostructures. Fig. 9 shows a diameter distribution histogram based on the CNT4 TEM image; The MWCNT in the CNT4 structure have mean diameter between 10 and 100 nm and a few tens of micrometers of a length. The diameters of MWCNT are mostly in the range of 20–40 nm.

Through the BET-BJH analysis, the macrostructure presented a small surface area (1136 m^2/g), much of the structure volume is occupied by pores [66]. It presents a medium pore volume of 0.076 cm^3/g and a medium diameter of 268 nm. These pores are classified as macropores [67]. According to the Archimedes method, 54.41% of the 3D structure volume is related to pores. The density is very reduced, 0.2272 g/cm^3. Elevated quantities of large pores allow the absorption of high volumes of substances in the structure.

The thermogram in Fig. 10 shows only one stage of decomposition for the CNT4 sample at temperatures between 450 and 650 °C, which is a typical result for MWCNT [68,69]. DTG showed only one exothermic transition peak at approximately 650 °C. It is known that amorphous carbon burns at temperatures lower than 580 °C to 600 °C; defect-free single wall CNT, at 600 °C to 620 °C; and pure MWCNTs with 10 layers and more, at 750 °C to 790 °C [70]. The reduction of exothermic transition of the produced MWCNTs is likely due the presence of defects on the MWCNT walls as shown in the HRTEM image (Fig. 8 h) [69]. It can be inferred that the difference between these final weight loss values, 73 wt%, is equal to the MWCNT content of the sample. Therefore, the remaining 27 wt% corresponds to $MgFe_2O_4$. The magnesium ferrite structure decompose at temperatures higher than 1200 °C as presented in the thermogram for $MgFe_2O_4$ (Fig. 5). No peaks related to amorphous phase burning were observed.

CNT4 presented a distinct higher MWCNT production compared to the other samples. The high density of MWCNT allowed the production of a MWCNT 3D macrostructure (Fig. 11b). 0,100 g of $MgFe_2O_4$ produced a 3D macrostructure of 0.770 g and 8.78 × 14 × 9.9 mm. The carbon volume and shape are related to the alumina boat (Fig. 11a). The CT4 catalyst can be used to produce a variety of MWCNT macrostructures. The carbon structures grow accordingly with the crucible boat volume and shape specifications.

Besides the surface area, another important parameter in spinel based powder catalysts is the spinel inversion degree. As presented in the XRD analysis (Fig. 1), the increasing of heat treatment temperature leads to higher degrees of structural order-disorder transitions [5]. These transitions cause inversions in the spinel. Thereby, the CNT4 elevated MWCNT production may not be related just to the CT4 high surface area. The CT3 and CT4 presented a small difference between surface areas (Fig. 2a). However, the MWCNT samples produced using these catalysts (CNT3 and CNT4) had a significant difference between the graphitization degrees (Fig. 6). This is explained by the elevated spinel inversion that occurs for samples treated at temperatures above 957 °C [46]. In the magnesium ferrite structure, magnesium has a covalent character and oxygen occupies positions of low mobility. This leads to high mobility of Fe^{3+} ions [5]. With increasing temperature, these ions receive enough energy to move around in the structure switching or occupying new positions in the crystal lattice.

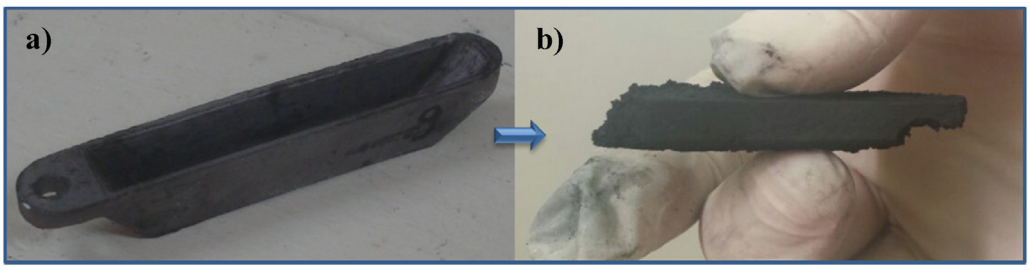

Fig. 11. a) 8.78 × 13.26 × 9.9 mm crucible boat used in the 3D macrostructure synthesis. b) Resulting 3D NTC macrostructure.

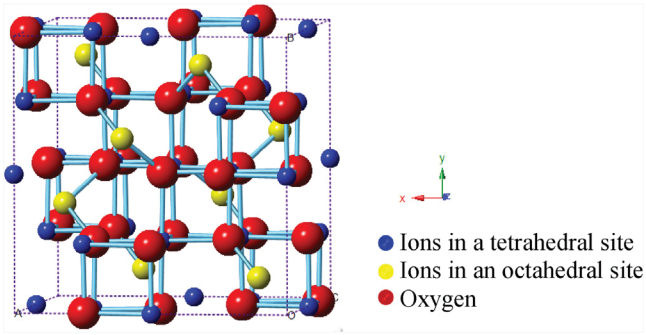

Fig. 12. Spinel ferrite Fd–3 m cubic crystalline structure. Representation of the ions occupying tetrahedral sites (blue), octahedral sites (yellow) and oxygen (red). (For interpretation of the references to colour in this figure legend, the reader is referred to the web version of this article.)

Fig. 12 presents the spinel ferrite Fd–3 m cubic structure. In a normal spinel structure, the divalent (A^{II}) ions occupy tetrahedral sites and the trivalent (B^{III}) ions occupy the octahedral sites in a close packed arrangement of oxide ions. A normal spinel can be represented as $(A^{II})^{tet}(B^{III})_2{}^{oct}O_4$. In an inverse spinel structure, the A^{II} ions occupy the octahedral sites, and part of the B^{III} ions occupy the tetrahedral sites. This can be represented as $(B^{III})^{tet}(A^{II}B^{III})^{oct}O_4$ [71].

In the $MgFe_2O_4$ lattice, with the increasing of heat treating temperature, gradually a higher number of Fe^{3+} ions moves to the tetrahedral sites. As shown at Fig. 12, these sites are located closer to the crystallite surface than the octahedral ones [72]. The spinel inversion allows more Fe^{3+} ions to be located on the crystallites surfaces; consequently, a higher quantity of Fe^{3+} is available on the particles surfaces. It increased the MWNTC production. In sample CNT5, despite the favorable positions of Fe^{3+} ions for catalytic activity, the MWCNT production was reduced. This result evidenced the strong influence of surface area on MWCNT production.

4. Conclusion

High purity and crystallinity $MgFe_2O_4$ nanoparticles were produced by SCS. The heat treatment study showed that the van der Waals forces strongly influenced particles at the nanoscale. The increase in crystallite size resulted reduced particle agglomeration, which increased the catalyst surface area. However, large particles lost surface area due their higher volume. The optimum crystallite size was settled. Samples treated at temperatures above 957 °C presented high ionic diffusion rates, which promotes elevated structural disorder and spinel inversions. As diffusion increases, the nanoparticles morphological changes are clearly observed. Nanospheres are seen at temperatures above 1100 °C. The CT4 sample showed the highest surface area, besides a high spinel inversion degree that favors the presence of Fe^{3+} ions on the nanoparticles surface. The CT4 catalyst produced a very dense MWCNT sample. This was successfully used to produce 3D MWCNT macrostructures. The volume and shape of these structures can be controlled by the crucible boat specifications. Nanoengineered 3D carbon structures with controlled density and architecture have great potential application in many areas including catalytic electrodes and environmental field.

Acknowledgments

The authors would like to thank the Coordination for the Improvement of Higher Education Personnel-CAPES for the financial support and the Microscopy and Microanalysis Center of Federal University of Rio Grande do Sul (CMM/UFRGS) for the technical support.

References

[1] Y. Ichiyanagi, M. Kubota, S. Moritake, Y. Kanazawa, T. Yamada, T. Uehashi, Magnetic properties of Mg-ferrite nanoparticles, J. Magn. Magn. Mater. 310 (2007) 2378–2380.
[2] Z. Wang, P. Lazor, H. St.C. Saxena, O' Neill, High pressure Raman spectroscopy of ferrite $MgFe_2O_4$, Mater. Res. Bull. 37 (2002) 1589–1602.
[3] Z.J. Zhang, Z.L. Wang, B.C. Chakoumakos, J.S. Yin, Temperature dependence of cation distribution and oxidation state in magnetic Mn-Fe ferrite nanocrystals, J. Am Chem. Soc. 120 (8) (1998) 1800–1804.
[4] C.S. Xavier, R.A. Candeia, M.I.B. Bernardi, S.J.G. Lima, E. Longo, C.A. Paskocimas, L.E.B. Soledade, A.G. Souza, I.M.G. Santos, Effect of modofier ion the properties of MgFe2O4 and ZnFe2O4 pigments, J. Therm. Anal. Calorim. 87 (3) (2007) 709–713.
[5] S.M. Antão, I. Hassan, J.B. Parise, Cation ordering in magnesioferrite, MgFe2O4, to 982 °C using in situ synchrotron X-ray powder diffraction, Am. Mineral. 90 (2005) 219–228.
[6] Y. Peng, Y. Yi, L. Li, H. Ai, X. Wang, L. Chen, Fe-based soft magnetic composites coated with NiZn ferrite prepared by a co-precipitation method, J. Magn. Magn. Mater. 428 (2017) 148–153.
[7] S. Hcini, A. Selmi, H. Rahmouni, A. Omri, M.L. Bouazizi, Structural, dielectric and complex impedance properties of $T_{0.6}Co_{0.4}Fe_2O_4$ (TNi Mg) ferrite nanoparticles prepared by sol gel method, Ceram. Int. 43 (2017) 2529–2536.
[8] J. Kurian, M.J. Mathew, A facile approach to the elucidation of magnetic parameters of CuFe2O4 nanoparticles synthesized by hydrothermal route, J. Magn. Magn. Mater. 428 (2017) 204–212.
[9] M. Junaid, M. AzharKhan, F. Iqbal, G. Murtaza, M. Akhtar, M. Ahmad, I. Shakir, M.F. Warsi, Structural,spectral,dielectric and magneticproperties of Tb-Dy doped Li-Ni nano-ferrites synthesized via micro-emulsion route, J. Magn. Magn. Mater. 428 (2017) 204–212.
[10] B. Pourgolmohammad, S.M. Masoudpanah, M.R. Aboutalebi, Effect of starting solution acidity on the characteristics of CoFe2O4 powders prepared by solution combustion synthesis, J. Magn. Magn. Mater. 424 (2017) 352–358.
[11] Z. Zhang, W. Wang, Solution combustion synthesis of CaFe2O4 nanocrystal as a magnetically separable photocatalyst, Mater. Lett. 133 (2014) 212–215.
[12] C.L. Yeh, C.H. Chiang, Effects of metal carbides as additives on combustion synthesis of $Ti_3(Al, Sn)C_2$ solid solutions, J. Alloys Compd. 694 (2017) 1154–1159.
[13] K.C. Patil, M.S. Hegde, S.T. Aruna, T. Rattan, Chemistry of Combustion Synthesis: Properties and Applications Nanocrystalline Oxide Materials, World Scientific Publishing Company Pte, India, 2008.
[14] Y. Huang, Y. Tang, J. Wang, Q. Chen, Synthesis of MgFe2O4 nanocrystallites under mild conditions, Mater. Chem. Phys. 97 (2006) 394–397.
[15] H. Xue, Z. Li, X. Wang, X. Fu, Facile synthesis of nanocristalline zinc ferrite via a self-propagating combustion method, Mater. Lett. 61 (2) (2007) 347–350.
[16] L. Satyanarayana, K.M. Reddy, S.V. Manorama, Nanosized spinel NiFe2O4 A novel material for the detection of liquefied petroleum gas in air, Mater. Chem. Phys. 82 (1) (2003) 21–26.
[17] P. Dinka, A.S. Mukasyan, In situ preparation of oxide based supported catalysts by solution combustion synthesis, J Phys. Chem. B. 109 (46) (2005) 21627–21633.
[18] P. Dubey, S.K. Choi, J.H. Choi, D.H. Shin, C.J. Lee, High-quality thin-multiwalled carbon nanotubes synthesized by Fe-Mo/MgO catalyst based on a solgel technique: synthesis, characterization, and field emission, J. Nanosci. Nanotechnol. 10 (2010) 3998–4006.
[19] T. Das, N. Arai, N. Sakamoto, K. Shinozaki, H. Suzuki, N. Wakiya, Impact of acidic catalyst to coat superparamagnetic magnesium ferrite nanoparticles with silica shell via sol–gel approach, Adv. Powder Technol. 27 (2016) 541–549.
[20] T. Kobayashi, Cancer hyperthermia using magnetic nanoparticles, Biotechnol. J 6 (2011) 1342–1347.
[21] J. Nonkumwong, P. Pakawanit, A. Wipatanawin, P. Jantaratana, S. Ananta, L. Srisombat, Synthesis and cytotoxicity study of magnesium ferrite-gold core-shell nanoparticles, Mater. Sci. Eng. C 61 (2016) 123–132.
[22] D.H.K. Reddy, Y.-S. Yun, Spinel ferrite magnetic adsorbents: alternative future materials forwater purification? Coord. Chem. Rev. 315 (2016) 90–111.
[23] A. Gruneis, M.H. Rummeli, C. Kramberger, A. Barreiro, T. Pichler, R. Pfeiffer, H. Kuzmany, T. Gemming, B. Buchner, High quality double wall carbon nanotubes with a defined diameter distribution by chemical vapor deposition from alcohol, Carbon 44 (2006) 3177–3182.
[24] Y. Wang, F. Wei, G. Luo, H. Yu, G. Gu, The large-scale production of carbon nanotubes in a nano-agglomerate fluidized-bed reactor, Chem. Phys. Lett. 364 (2002) 568–572.
[25] G. Ning, F. Wei, Q. Wen, G. Luo, Y. Wang, Y. Jin, Improvement of Fe/MgO catalysts by calcination for the growth of single- and double-Walled carbon nanotubes, J. Phys. Chem. B. 110 (3) (2006) 1201–1205.
[26] Q.W. Li, H. Yan, Y. Cheng, J. Zhang, Z. Liu, A scalable CVD synthesis of high-purity single-walled carbono nanotubes with porous MgO as support material, J. Mater. Chem. 12 (4) (2002) 1179–1183.

[27] Q. zhang, M. Zhao, J. Huang, W. Qian, F. Wei, Selective synthesis of single/Double/Multi-walled carbon nanotubes on mgO-Supported Fe catalyst, Chin. J. Catal. 29 (11) (2008) 1138–1144.
[28] Y. Wang, F. Wei, G. Luo, H. Yu, G. Gu, The large-scale production of carbon nanotubes in a nano-agglomerate fluidized-bed reactor, Chem. Phys. Lett. 364 (2002) 568–572.
[29] B. Tran, J.-F. Colomer, J.-P. Pirard, S. Lambert, Carbon nanotubes synthesis by the ethylene chemical catalytic vapour deposition (CCVD) process on Fe, Co, and Fe–Co/Al_2O_3 sol–gel catalysts, Appl. Catal., A 318 (2007) 63–69.
[30] E. Flahaut, C. Laurent, A. Peigney, Catalytic CVD synthesis of double and triple-walled carbon nanotubes by the control of the catalyst preparation, Carbon 43 (2005) 375–383.
[31] S. Ozden, T.N. Narayanan, C.S. Tiwary, P. Dong, H.C. Hart, R. Vajtai, P.M. Ajayan, 3D macroporous solids from chemically crosslinked carbon nanotubes, Small 11 (2015) 688–693.
[32] N. Iqbal, X. Wang, A.A. Babar, J. Yu, B. Ding, Highly flexible NiCo2O4/CNTs doped carbon nanofibers for CO2 adsorption and supercapacitor electrodes, J. Colloid Interface Sci. 476 (2016) 87–93.
[33] X. Fan, T. Wang, Y. Guo, H. Gong, H. Xue, H. Guo, B. Gao, J. He, Synthesis of ordered mesoporous TiO_2-Carbon-CNTs nanocomposite and its efficient photoelectrocatalytic methanol oxidation performance, Microporous Mesoporous Mater. 240 (2017) 1–8.
[34] M.C. Serrano, M.C. Gutiérrez, F. del Monte, Role of polymers in the design of 3D carbon nanotube-based scaffolds for biomedical applications, Prog. Polym. Sci. 39 (2014) 1448–1471.
[35] Y. Penga, K. Wang, M. Yuc, A. Lia, R.K. Bordiad, An optimized process for in situ formation of multi-walled carbon nanotubes in templated pores of polymer-derived silicon oxycarbide, Ceram. Int. 43 (2017) 3854–3860.
[36] X. Gui, H. Li, K. Wang, J. Wei, Y. Jia, Z. Li, L. Fan, A. Cao, H. Zhu, D. Wu, Recyclable carbon nanotube sponges for oil absorption, Acta Mater. 59 (2011) 4798–4804.
[37] D.P. Hashim, N.T. Narayanan, J.M. Romo-Herrera, D.A. Cullen, M.G. Hahm, P. Lezzi, J.R. Suttle, D. Kelkhoff, E. Munõz-Sandoval, S. Ganguli, A.K. Roy, D.J. Smith, R. Vajtai, B.G. Sumpter, V. Meunier, H. Terrones, M. Terrones, P.M. Ajayan, Covalently bonded three-dimensional carbon nanotube solids via boron induced nanojunctions, Sci. Rep. 2 (2012) 363–371.
[38] A. Siddiqa, A. Shahid, R. Gill, Silica decorated CNTs sponge for selective removal of toxic contaminants and oil spills from water, J. Environ. Chem. Eng. 3 (2015) 892–897.
[39] S. Ozden, L.D. Machado, C. Tiwary, P.A.S. Autreto, R. Vajtai, E.V. Barrera, D.S. Galvao, P.M. Ajayan, Ballistic fracturing of carbon nanotubes, ACS Appl. Mater. Interfaces 8 (2016) 24819–24825.
[40] S. Ozden, C.S. Tiwary, A.H.C. Hart, A.C. Chipara, R. Romero-Aburto, M.-T.F. Rodrigues, J. Taha-Tijerina, R. Vajtai, P.M. Ajayan, Density variant carbon nanotube interconnected solids, Adv. Mater 27 (2015) 1842–1850.
[41] R. Koizumi, A.H.C. Hart, G. Brunetto, S. Bhowmick, P.S. Owuor, J.T. Hamel, A.X. Gentles, S. Ozden, J. Lou, R. Vajtai, S.A. Syed Asif, D.S. Galvão, C.S. Tiwary, P.M. Ajayan, Mechano-chemical stabilization of three-dimensional carbon nanotube aggregates, Carbon 110 (2016) 27–33.
[42] A.M. Baker, L. Wang, S.G. Advani, A.K. Prasad, Nafion membranes reinforced with magnetically controlled Fe_3O_4–MWCNTs for PEMFCs, J. Mater. Chem 22 (2012) 14008–14012.
[43] S.R. Jain, K.C. Adiga, A new approach to thermochemical calculations of condensed fuel-Oxidizer mixtures, Combust. Flame 40 (1981) 71–79.
[44] T.L. Heath, The Method of Archimedes, Cambridge the University Press, London, 1912.
[45] G. Effenberg, S. Ilyenko, Ternary Alloy Systems Phase Diagrams, Crystallographic and Thermodynamic Data, Springer, Berlin Heidelberg, German, 2008.
[46] K.R. Bonnickson, High temperature heat contents of calcium and magnesium ferrites, J. Am. Chem. Soc. 76 (6) (1954) 1480–1482.
[47] N.M. Deraz, O.H. Abd-Elkader, Effects of magnesia content on spinel magnesium ferrite formation, Int. J. Electrochem. Sci. 8 (2013) 8632–8644.
[48] H.E. Ries, R.A. Van Nordstrand, J.W. Teter, Surface area of catalysts, Ind. Eng. Chem. 1945 37 (4) (1945) 310–317.
[49] R.M. Rioux, H. Song, J.D. Hoefelmeyer, P. Yang, G.A. Somorjai, High-Surface-Area catalyst design: synthesis, characterization, and reaction studies of platinum nanoparticles in mesoporous SBA-15 silica, J. Phys. Chem. B 109 (2005) 2192–2202.
[50] K.H. Müller, M. Motskin, A.J. Philpott, A.F. Routh, C.M. Shanahan, M.J. Duer, J.N. Skepper, The effect of particle agglomeration on the formation of a surface connected compartment induced by hydroxyapatite nanoparticles in human monocyte-derived macrophages, Biomaterials 35 (2014) 1074–1088.
[51] D. To, R. Dave, X. Yin, S. Sundaresan, Deagglomeration of nanoparticle aggregates via rapid expansion of supercritical or high-Pressure suspensions, AIChE J. 55 (2009) 2807–2826.
[52] A.A. Kozulin, S.A. Vorozhtsov, S.S. Kulkov, U. Teipel, S.N. Kulkov, Ultrasonic deagglomeration of aluminum nanopowders with multi-walled carbon nanotube mixtures, AIP Conference Proceedings. 1683 (2015), 020102(1–4).
[53] P.A. Hartley, G.D. Parfitt, L.B. Pollack, The role of the van der Waals force in the agglomeration of powders containing submicron particles, Powder Technol. 42 (1) (1985) 35–46.
[54] R. Lee-Desautels, Theory of van der waals forces as applied to particlate materials, Educ. Reso. for Part. Techn 051 (2005) 1–6.
[55] E.M. Hotze, T. Phenrat, G.V. Lowry, Nanoparticle aggregation: challenges to understanding transport and reactivity in the environment, J. Environ. Qual. 39 (6) (2010) 1909–1924.
[56] J. Yun, C.-H. Jung, D. Park, H.Y. Koo, J.-Y. Yun, Y. Kim, J. Young Park, The effect of loading on sintering and catalytic activity of Pt/SiO_2 hybrid catalyst powders synthesized via spray pyrolysis, Korean J. Chem. Eng. 31 (11) (2014) 1980–1984.
[57] R.K. Sharma, P. Sharma, A. Maitra, Size-dependent catalytic behavior of platinum nanoparticles on the hexacyanoferrate(III)/thiosulfate redox reaction, J. Colloid Interface Sci. 265 (2003) 134–140.
[58] M. Torii, T. Kosaka, T. Maeda, H. Rikukawa, Low Temperature Sinterable Oxide Magnetic Material, United States Patent(4, 540, 500), 1985.
[59] S. Navarro, R.T. Noyes, The Mechanics and Physics of Modern Grain Aeration Management, CRC Press ed., United States of America, 2002.
[60] M.P. Reddy, X.B. Zhou, Q. Huang, R.R. Reddy, Synthesis and characterization of ultrafine and porous structure of magnesium ferrite nanospheres, Int J Nano Stud Technol. 3 (6) (2014) 72–77.
[61] H. Aono, H. Hirazawa, T. Naohara, T. Maehara, Surface study of fine $MgFe_2O_4$ ferrite powder prepared by chemical methods, Appl. Surf. Sci. 254 (2008) 2319–2324.
[62] M. Kubota, Y. Kanazawa, K. Nasu, S. Moritake, H. Kawaji, T. Atake, Y. Ichiyanagi, Effect of treatment on magnetic $Mgfe_2O_4$ nanoparticles, J. Therm. Anal. Calorim. 92 (2) (2008) 461–463.
[63] R.A. Dileo, B.J. Landi, R.P. Raffaelle, Purity assessment of multiwalled carbon nanotubes by Raman Spectroscopy, J. Appl. Phys. 101 (2007) 1–5.
[64] R. Saito, A. Gruneis, Ge. G. Samsonidze, V.W. Brarr, G. Dresselhaus, et al., Double resonance Raman spectroscopy of single-wall carbono nanotubes, New J. Phys. 5 (2003), 157. 1–157.15.
[65] A. Yasuda, N. Kawase, F. Banhart, W. Mizutani, T. Shimizu, H. Tokumoto, Graphitization mechanism during the carbon-Nanotube formation based on the In-Situ HRTEM observation, J. Phys. Chem. B. 106 (2002) 1849–1852.
[66] P.B. Sarawade, J.-K. Kim, H.-K. Kim, H.-T. Kim, High specific surface area TEOS-based aerogels with large pore volume prepared at an ambient pressure, Appl. Surf. Sci. 254 (2007) 574–579.
[67] B.-L. Su, C. Sanchez, X.-Y. Yang, Hierarchically Structured Porous Materials, Wiley-VCH Verlag & Co KGaA, Germany, 2012.
[68] W.M. Silva, H. Ribeiro, L.M. Seara, H.D.R. Calado, A.S. Ferlauto, R.M. Paniago, C.F. Leite, G.G. Silva, Surface properties of oxidized and aminated multi-Walled carbon nanotubes, J. Braz. Chem. Soc. 23 (6) (2012) 1078–1086.
[69] B. Scheibe, E. Borowiak-Palen, R.J. Kalenczuk, Oxidation and reduction of multiwalled carbon nanotubes —preparation and characterization, Mater. Charact. 61 (2010) 185–191.
[70] V.A. Labunov, A.S. Basaev, B.G. Shulitski, Y.P. Shaman, I. Komissarov, A.L. Prudnikava, B.K. Tay, M. Shakerzadeh, Growth of few-wall carbon nanotubes with narrow diameter distribution over Fe-Mo-MgO catalyst by methane/acetylene catalytic decomposition, Nanoscale Res. Lett. 7 (2012) 102.
[71] R.J.D. Tilley, Understanding Solids, John Wiley & Sons Ltd, England, 2004.
[72] M. Gateshki, V. Petkov, S.K. Pradhan, T. Vogt, Structure of nanocrystalline $MgFe_2O_4$ from X-ray diffraction, Rietveld and atomic pair distribution function analysis, J. Appl. Cryst. 38 (2005) 772–779.